Available online at www.sciencedirect.com
ScienceDirect
Acta Biomaterialia 2 (2006) 595–607
Acta BIOMATERIALIA
www.actamat-journals.com

Equal and local-load-sharing micromechanical models for collagens: Quantitative comparisons in response of non-diabetic and diabetic rat tissue

Bradley E. Layton [a], Ann Marie Sastry [a,b,*]

[a] Department of Mechanical Engineering, Drexel University, Philadelphia, PA, USA
[b] Department of Mechanical Engineering, University of Michigan, 2140 GGBrown, 2350 Hayward Street, Ann Arbor, MI 48109-2125, USA

Received 23 February 2006; received in revised form 9 May 2006; accepted 17 May 2006

Abstract

Chemical crosslinks in collagens resulting from binding of advanced glycation end-products, have long been presumed to alter the stiffness and permeability of glycated tissues. Recently, we developed a stochastic mechanical model for the response and failure of uniaxially deformed sciatic nerve tissue from diabetic and control rats. Here, we use our model to determine the likely correlation of fibril glycation with failure response, by quantifying statistical differences in their response. Our four-parameter model describes both the non-linear toe region and non-linear failure region of these tissues; the four parameters consist of (1) collagen fibril alignment, (2) fiber bundle waviness, (3) Weibull shape parameter for fibrillar strength, and (4) modulus-normalized Weibull scale parameter for fibrillar strength. Using an equal load sharing model we find that diabetic and control tissues had shape parameters of 9.88 ± 5.50 and 4.33 ± 3.67 ($p = 0.043$), respectively, and scale parameters of 0.28 ± 0.07 and 0.58 ± 0.25 ($p = 0.033$), respectively, implying that the diabetic tissue behaves in a more brittle manner, consistent with more highly crosslinked fibrils. We conclude that biochemical crosslinking directly affects measured mechanical properties. Further, this mechanical characterization may prove useful in mapping alterations in stiffness and permeability observed in glycated tissues.
© 2006 Acta Materialia Inc. Published by Elsevier Ltd. All rights reserved.

Keywords: Nerve; Mechanics; Collagen; Diabetes; ECM

1. Introduction

A clear pathway from the binding of advanced glycation end-products (AGEs) to alterations in the mechanical response of collagenous tissue has not yet been directly established, though they are clearly linked. Glycation-induced crosslinkings of fibrillar collagens of types I, III, V and XI [2–7] have been implicated, for example, in stiffening of skin [8,9] and reduced fracture toughness in bone [10]. Greater duration and intensity of exposures to glucose have been shown to amplify the effects of collagen glycation [11–13].

Nerve tissue contains ~10–16% collimated collagen by mass fraction [14–16]. This tissue undergoes glycation [17,18], and exhibits altered mechanical properties, which can be modeled using micromechanics [18,19]. The gross mechanical properties of peripheral nerve [20,21] and collagen fibrils [22,23] have been quantified, but until our own work, there was apparently no model correlating glycation with mechanical properties at the tissue scale. Our methodology [18,19] was an application of classical bundle theory, applied to the fibrillar collagen of the nerve sheath [24–26]. The model was developed for the fibril scale (Fig. 1), at which the individual fibrils may be modeled as spatially periodic and finite in length. The concept underlying this

* Corresponding author. Address: Department of Mechanical Engineering, University of Michigan, 2140 GGBrown, 2350 Hayward Street, Ann Arbor, MI 48109-2125, USA. Tel.: +1 734 764 3061; fax: +1 734 647 3170.
E-mail address: amsastry@engin.umich.edu (A.M. Sastry).

1742-7061/$ - see front matter © 2006 Acta Materialia Inc. Published by Elsevier Ltd. All rights reserved.
doi:10.1016/j.actbio.2006.05.013

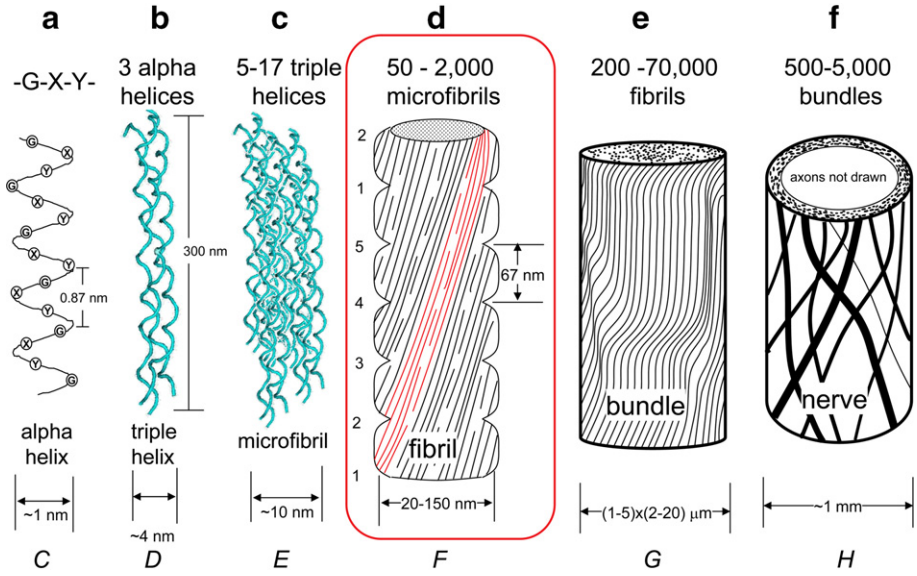

Fig. 1. A series of figures from molecular scale to tissue scale. The letters *C–H* correspond to failure functions [24,25] used to predict failure at a larger scale based on known properties at a smaller scale. The function *F* was chosen to represent the fibril scale and is the scale of interest for the present work. In (a) a left-handed triple helix of a fibrillar collagen is depicted with glycine occupying every third position, see e.g., Refs. [81,82]. In (b) three triple helices, see e.g., Ref. [83], self-assemble into (c) microfibrils of varying size prior aggregating into (d) fibrils [55,84]. These fibrils are then organized into (e) wavy tape-like bundles in the epineurium that encase (f) whole nerve [50,85]. Dimensions given for fibrils, bundles and whole nerve are those of rat sciatic nerve.

present work is based on weakest-link scaling: a structure comprised of distinct subcomponents placed in series fails when one subcomponent fails. For structures comprised of parallel subcomponents, all subcomponents in a given link must fail before the entire structure fails. Here, we model nerve tissue as a set of load-supporting collagen fibrils in parallel.

More generally, the order in which neighbors of broken fibrils rupture depends upon the nature of the "matrix;" in this case, the matrix is the ground substance, which can be assumed to have negligible mechanical effect in collimated, collagen-reinforced nerve tissues. For glycated tissues, however, collagens can be assumed to exhibit substantial crosslinking under these conditions, and so, the effect is similar to that of a matrix of low contrast ratio to the reinforcing phase (i.e., similar mechanical modulus). One extreme strategy for modeling sequential rupture in such a material is to assume that all surviving fibrils carry load equally (equal load sharing, or ELS). The other extreme is to assume that only the fibrils in the immediate vicinity of the broken fibril assume all overload (an example of local load sharing, or LLS). These models correspond, respectively, to a matrix of low or high contrast ratio. With glycation, it can be reasonably hypothesized that response of collimated collagens would be closer to LLS, due to increased correlation of fibrils.

In this work, we present a parametric constitutive failure model for peripheral nerve, to test this hypothesis, using the following key variables: fibril waviness, as defined by the ratio between the spatial amplitude and fibril periodicity, fibril angle with respect to the primary tissue axis, Weibull shape parameter, and Weibull scale parameter. Other variables included are collagen fibril modulus, tissue scale collagen density, and microscale packing density [19]. The model is capable of capturing the full behavior of the non-linear behavior of the nerve tissue from the toe region, through the linear region and up to failure. The fibril waviness and fibril angle capture the shape of the toe region, while the Weibull scale and shape factors describe the failure region.

1.1. AGE binding of collagens

The basis for the presumably increased mechanical correlation of glycated fibrils is the known increase in AGE binding in blockage of binding sites of extracellular matrix (ECM) proteins such as collagen IV and laminin, impeding cell adhesion, growth, and tissue remodeling [27]. AGE-specific fluorescence and enzyme-linked immunosorbent assay (ELISA)-based binding have been shown to increase with time in the coronary collagen of diabetes-induced rats [28]. ELISA and solubility assays have been used to show that collagen crosslinks form both in the presence and absence of either free glucose or oxygen or a combination of glucose and oxygen [4]. Overall, extensive chromatography experiments with high performance liquid chromatography have resulted in the identification of over 30 distinct AGEs [29,30]. Indeed, the presence of AGEs coincident with glucose exposure has been shown to stiffen human skin exposed to glucose-6-phosphate *in vitro* by as much as 80% [9] and rat tail tendon by 100% [31] *in vitro*, and to diminish stiffness by 50% and strength by 29% in healing rat femoral bone, *in vivo* [10]; the crosslinks that are presumably responsible for stiffening skin are also responsible

for reducing the repair rate in bone by altering the kinetics of collagenases as well as collagen self-assembly mechanisms responsible for tissue remodeling.

1.2. Measurements in diabetic tissues: prior art

Collagen upregulation has been measured in explanted human fibroblasts in the presence of diabetic-level glucose concentrations, *in vitro*, at both the translation and transcription levels for Type III collagen and fibronectin, but not Type I [32]. Upregulation has also been documented *in vivo* in rat skin studies, where higher glucose concentrations in diabetic animals have been implicated in higher, non-specific collagen concentrations, based on hydroxyproline levels. Upregulated Type I collagen and fibronectin with elevated glucose concentrations has also been measured in explanted sciatic rat nerve tissue, via Northern hybridization [33]. Type VI collagen accumulation in diabetic human and rat nervous tissues has further been quantified by immunoelectron microscopy; Type IV translation upregulation has been quantified in rat neural cells [34].

Morphologically, collagen fibril diameter enlargement has also been quantified in a number of models for diabetes. In an *in vivo* rat model, larger-than-normal, non-specific (Type I/Type III) collagen fibril diameters were measured in diabetic rat endoneurium via transmission electron microscopy (TEM) [35]. This was also found *in vivo* in diabetic humans with TEM [36], and both *in vivo* and *in vitro* with rat tail tendon with atomic force microscopy (AFM) [3] and finally, *in vitro* in endoneurium and epineurium in two diabetic rat models with AFM [17].

These morphological alterations are presumed to result from AGE binding and subsequent irreversible crosslinking of collagen. Collagen has naturally occurring crosslinks in the form of dehydrohydroxylysinonorleucine [37,38]. Portions of the collagen molecule, not typically crosslinked by lysyl oxidase, however, can become irreversibly crosslinked in the presence of glucose [39–41]. When exposed *in vitro* to reducing sugars such as glucose, ribose and glyceraldehydes, rat tail tendon has shown a radial expansion of collagen fibril lattice, due to covalent bonding of the sugar with the lysyl and hydroxylysyl groups of the collagen, leading to crosslinks [42].

In recent work using liquid chromatography/mass spectroscopy, over 20 advanced glycation end products, in particular those forming crosslinks such as GOLD (glyoxal-derived lysine dimer), MOLD (methylglyoxal-derived lysine dimer), and DOLD (3-deosyglucosone-derived lysine dimer) were quantified in human blood plasma samples [43]. If such a technique could be used to account for all crosslinks in structural proteins such as collagen, a non-destructive or minimally invasive method for assessing AGE concentration could be used to predict mechanical properties in heavily glycosylated tissue.

Methods such as detection with fluorescence or autofluorescence have also been used to determine the relative concentrations of various AGEs, see e.g., Ref. [44], though the biochemistry of these crosslinks has not been fully elucidated. Fluorescence emission has been correlated with intermolecular spacing in corneal collagen; fluorescent emission increased with age as did intermolecular spacing, presumably due to an increase in crosslink density [45]. More recent work [46] has employed an immunochemical detection method to detect AGEs. And most recently a positive correlation has been shown [47] between autofluorescence in skin at that 440 nm range and the amount of pentosidine, a known crosslinking agent [48]. However, the absorption spectra investigated may have overlapped with that of other fluorophores such as nicotinamide adenine dinucleotide (NADH) and hemoglobin.

1.3. Modeling and hypotheses

Though we expect glucose-induced crosslinking to produce classically altered mechanical response in collagen-reinforced tissue, our prior work [18] showed no significant differences in mechanical response between diabetic and control tissues up to 40% strain. This strain is nearly coincident with the strain required to ''straighten'' collagen fibers, which exhibit significant waviness; we may presume that after this point, the mechanics of the actual crosslinks are investigated.

In the present work, we perform simulations and experiments to determine the behavior of the collagens surrounding nerve tissue. Our hypotheses are:

(1) Diabetic nerve tissues exhibit significantly greater shape parameters than normal nerve tissues. Qualitatively, this means that the stress–strain curve of the diabetic tissue will be more sharply peaked at failure.
(2) Diabetic nerve tissues exhibit significantly lower failure-stress-to-modulus ratios than normal nerve tissues.
(3) A local load sharing rule will have a better goodness-of-fit for the stress–strain responses of diabetic nerve than controls; conversely, the equal load sharing rule will produce stress–strain responses that fit the control curves better than the diabetic curves.

2. Methods

Our model employs the Weibull distribution as developed classically [49] and as later applied to composite materials [24,25], assuming parameters at the fibril scale (Fig. 1d, Table 1). Data from our own experiments on whole rat sciatic nerve from diabetic and control animals [18,19] were compiled for model input. Prior to this, published collagen images [50] were analyzed to guide our estimations of collagen fibril bundle morphology. Published failure strengths of collagen fibrils were found to range from 2 to 70 MPa [22,51,52]. Collagen fibril stiffnesses were also taken from the literature, for reassembled fibrils (1–6 MPa) [53] and bovine Achilles tendon (430 MPa) [22]. Data on the molecular structure of collagen fibrils, such

Table 1
Size scales in collagenous structure of peripheral nerve

Structure	In-plane dimension	Axial dimension	Load sharing notation	Series elements (m)	Parallel elements (n)
Amino acids	1 nm	0.5 nm			
Alpha helices	1.4 nm	300 nm	C	1400	1
Triple helices	4 nm	300 nm	D	1	3
Microfibril	10 nm	600 nm	E	1	5–17
Fibril	20–150 nm	<1 mm	F	10,000	50–2000
Bundle	(1–5) × (2–20) μm	<10 mm	G	1	200–70,000
Nerve	1 mm	<20 mm	H	1	500–5000

Values for m and n represent the number of structural elements from the preceding structural scale that comprise the given structure. For example, approximately 5–17 fibrils comprise a microfibril in parallel and a microfibril has length on the order of one triple helix. Values given for collagen fibril diameter, bundle dimension, and nerve diameter are for rat sciatic nerve.

as the three-dimensional packing order, were taken from published values determined via X-ray diffraction [54,55].

We made the following assumptions in our model for whole-nerve response: (1) collagen fibrils are contiguous within a typical (~10 mm) tissue sample (Fig. 2); (2) the fibril scale is the functional scale for stiff elements within the tissue; (3) fibril waviness can be modeled adequately as finite and periodic functions; and (4) the load-sharing interdependence of fibrils can be assumed to fall within the extreme bounds of ELS and LLS. Also, the following assumptions were implicit in our model: (1) crosslinks within triple helices affect the axial properties; and (2) tissues containing larger-diameter fibrils are not necessarily stiffer, since the larger diameters result mainly from decorations of ECM proteins (Fig. 3) such as Amadori products [56], and do not affect the backbone stiffness.

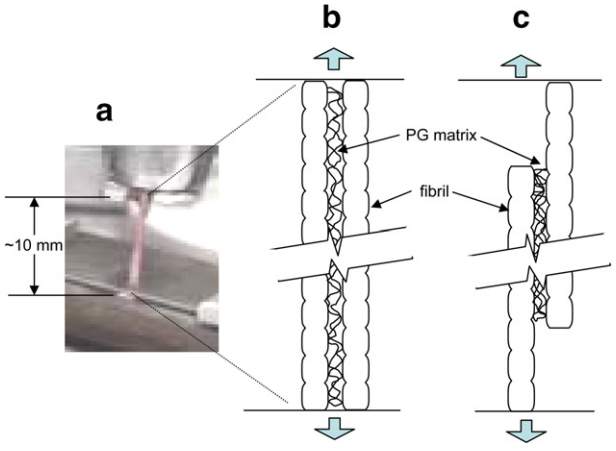

Fig. 2. A schematic of two possible mechanisms for load transfer within collagenous tissue: (a) photograph of rat sciatic nerve being tested uniaxially for the current study shows (b) load transferred solely within fibrils vs. (c) load transferred via shear within matrix among fibrils. Adapted from Ref. [86].

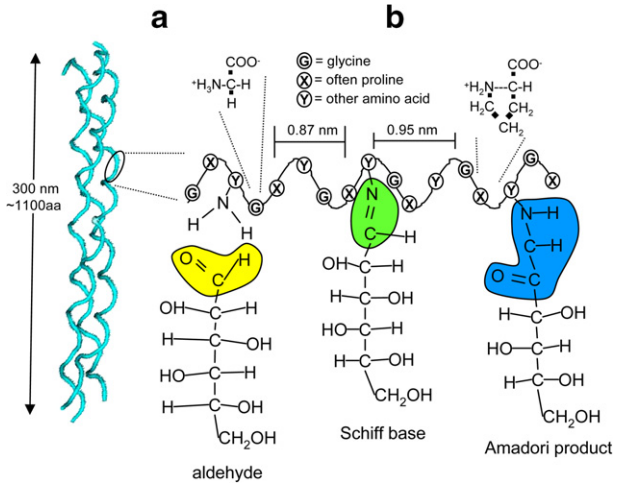

Fig. 3. A molecular view of collagen, where three left-handed helices form a right-handed triple helix held together by hydrogen bonds (http://www.ncbi.nlm.nih.gov/). At the secondary scale of collagen, where left-handed alpha helices form and glucose, or another monosaccharide, may spontaneously form a open-loop structure, freeing an aldehyde which has the potential to form a Schiff base and finally an Amadori product or advanced glycation end-product (AGE) [30] with one of the over 1000 nitrogen atoms of each collagen molecule which occupy every third atomic position of the peptide chain.

Tissue response was simulated by selecting values for the following parameters (Table 2): average fibril modulus, $\overline{E}_f$, collagenous area of nerve, A_c, packing fraction of collagen, f, average, $\bar{\gamma}$, and standard deviation, σ_γ, of collagen fibril bundle angle, γ, average, $\bar{a}$, and standard deviation, σ_a, of collagen fibril amplitude, a, Weibull modulus, x_0, and Weibull shape parameter, α. Ideally, $\overline{E}_f$, A_c and f are known for a given tissue sample *a priori*. In this work, A_c was set to 0.1, which is near the lower end of the literature values; for example, a value of 0.106 was reported for human pelvic cavity nerve [14], a value of 0.16 was found by for human posterior tibial nerve [15] and a value of ~0.15 was reported for adult Sprague–Dawley rat sciatic nerves [16]. The packing fraction of collagen within the collagenous portion, f, was set to 0.7, an approximation made after analysis of images of diabetic and non-diabetic BioBreeding rats [35], the same species used in this study. The value of $\overline{E}_f$ was taken directly from data from our own uniaxial stress–strain experiments, and calculated from

$$E_f = A_c f \frac{\sigma_H - \sigma_L}{\varepsilon_H - \varepsilon_L}, \tag{1}$$

for each tissue specimen, where ε_L and σ_L represent the lower deviation from linearity on the stress–strain curve and ε_H and σ_H represent the upper deviation from linearity.

Sinusoidal fibrils were modeled as 10 connected line segments, denoted by vectors

$$u = \{0, 0.1, 0.2, \ldots, 1.0\}, \ldots, 2\pi, \quad \text{and} \tag{2}$$

$$v = a \sin u, \tag{3}$$

Table 2
Measured, estimated and calculated parameters used as input to the mechanical model of peripheral nerve

	Parameter	Value	Description
Measured	D_N	~1 mm	Whole nerve diameter
	ε_L	0.07–0.37	Lower strain limit of linear portion of stress–strain curve
	ε_H	0.15–0.63	Upper strain limit of linear portion of stress–strain curve
	σ_L	0.15–0.63	Lower stress limit of linear portion of stress–strain curve
	σ_H	0.15–0.63	Upper stress limit of linear portion of stress–strain curve
	E_N	4–50 MPa	Elastic modulus of whole nerve
Estimated	A_c	0.1	Area fraction of collagenous portion of nerve
	f	0.7	Area packing fraction of collagen within collagenous portion of nerve
Calculated	E_F	100–500 MPa	Elastic modulus of collagen fibrils
Model	$\bar{\gamma}$	0	Average fibril angle in radians (zero for all simulations)
	σ_γ	0–0.82	Standard deviation of fibril angle in radians (0 = parallel to nerve axis)
	$\bar{a}$	0–1	Fibril amplitude normalized to fibril sinusoidal spatial wavelength
	σ_a	0–0.35	Standard deviation of fibril amplitude
	E_x	0–1	Normalized fibril Weibull scale parameter strength/modulus
	α	0–10	Fibril Weibull shape parameter

Measured parameters were taken directly from uniaxial tension stress–strain curves of whole sciatic nerves from BioBreeding rats [18]. Estimated value for A_c was taken from [14]. Estimated value for f was taken from [35]. The value for E_f was calculated based on Eq. (1) and is used to match the linear region of the stress–strain curve. Of the parameters used to define the model, $\bar{\gamma}$, σ_γ, $\bar{a}$, σ_a describe the shape of the toe region and the final two E_x and α describe the shape of the failure region.

where a is absolute fibril spatial amplitude. To simulate the angle, γ, each fibril makes with the nerve axis, each fibril was rotated via

$$\begin{pmatrix} u' \\ v' \end{pmatrix} = \begin{pmatrix} \cos\gamma & -\sin\gamma \\ \sin\gamma & \cos\gamma \end{pmatrix} \begin{pmatrix} u \\ v \end{pmatrix}, \tag{4}$$

prior to simulated straining.

Eleven fibrils were used in each simulation; this value produced a satisfactorily smooth toe region stress–strain match with experimental results, and also resulted in a tractable computation (1–10 s on the computation platform described at the end of this section). Greater angles required longer computation times. Since statistics for both normalized fibril amplitude, a, and fibril angle, γ, affect the simulated toe-region shape independently, in our simulations we systematically varied the non-dimensionalized parameter, $\bar{a}$, from 0 to 1, in increments of 0.025,

$$\bar{a} = \frac{A}{L}, \tag{5}$$

where L is the fibril period. Angle standard deviation, σ_γ, was varied from 0 to ~0.85 (radians) in 40 increments, following our prior work [19].

This range was found to be sufficient to cover the entire range to minimize root mean square (RMS) error between simulated and experimental curves. Though solutions minimizing RMS error are frequently non-unique, i.e., there are several combinations of $\bar{a}$ and σ_a or $\bar{a}$ and σ_γ that map to a given RMS error, for the two domain variables, $\bar{a}$ and σ_a or $\bar{a}$ and σ_γ, the RMS error is single-valued. We bounded the combinations of these variables that minimized within 2.5% (40 values per axis) of the range of values of physiological interest for this tissue. To verify that a local minimum was not mistaken for the global minimum, several simulations with four times the discretization in each dimension were run. Simulations only up to ε_H (Fig. 4) were run to fit $\bar{a}$ and σ_a in one simulation set, then combinations of $\bar{a}$ and σ_γ that minimized RMS error in a second simulation set were found. In this manner, we were assured of bounding all reasonable values of our geometry variables. For example, curve 1 in Fig. 4 has a relatively smaller $\bar{a}$ or σ_γ than curve 3. Fig. 5 depicts a typical constitutive response from a control and a diabetic sample, and demonstrates the ability of the combined fibril-scale morphology stochastic failure prediction model to capture and parameterize behaviors as diverse as those shown.

Once the toe region was mapped with $\bar{a}$ and σ_a or $\bar{a}$ and σ_γ we used the Weibull distribution to model the fibril strength distribution according to

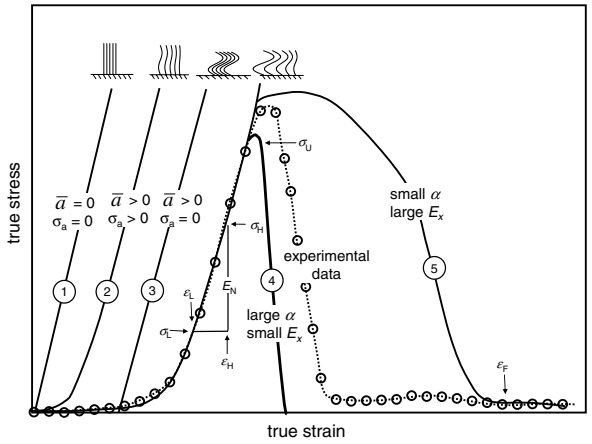

Fig. 4. A family of curves depicting the effects of average fibril amplitude, $\bar{a}$, and fibril amplitude standard deviation, σ_a (four leftmost curves) on the behavior of the toe region. The two rightmost solid curves depict the effects of the Weibull shape, α, and scale, E_x parameters on model results for matching uniaxial tension stress–strain curves for whole rat sciatic nerve. Generally, large α and large E_x result in a high, tight failure peak, whereas a small α and small E_x result in a low, broad failure plateau.

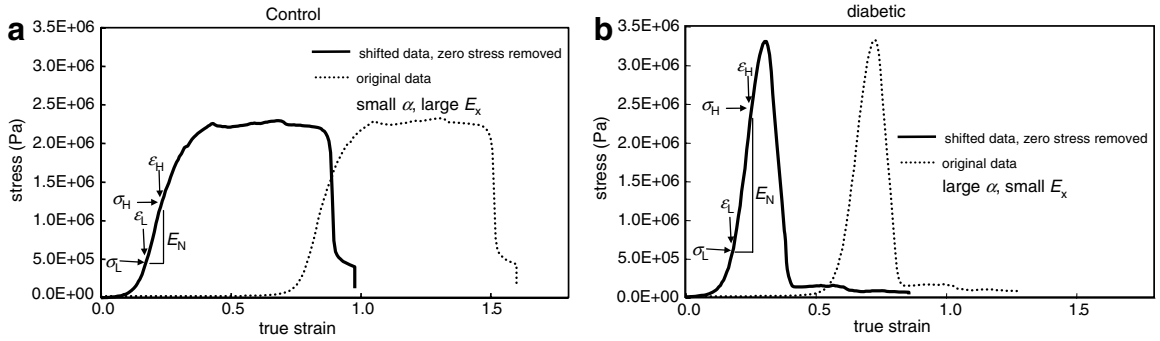

Fig. 5. Representative failure stress–strain curve from (a) control and (b) diabetic whole nerve uniaxial tests depicting strain limits, ε_L and ε_H of linear portion of curve used to determine whole nerve modulus, E_N. Initial toe region stress data points less than 0.5% of maximum stress were removed since data were taken from nerves which had been strained to 10%, 20%, 40%, and 80% prior to being stretched to failure. Vertical post-failure tail of control curve resulted from termination of test prior to complete tissue separation.

$$F(x) = 1 - e^{-\left(\frac{x}{x_0}\right)^{\alpha}}, \tag{6}$$

where x_0 and α, are scale and shape parameters, respectively. We determined the ranges of x_0 and α that produced RMS minima for all experimental curves, by extending them until global minima were found. Global minima for each case were inspected visually to verify that the numerical best fit matched the constitutive curve. To reduce excessive computation time and minimize spurious results resulting from running simulations to total failure strain ε_F (Fig. 4), simulations were run to a stress, σ_U, defined as 95% of the maximum stress attained in the experimental data. For convenience, x_0 was normalized to fibril modulus, E_f and fibril strength, E_x, was defined as

$$E_x = \frac{x_0}{E_f}. \tag{7}$$

It is well established that a composite material with many, small independent load-carrying members is less likely to fail abruptly than one with a few large members whose overload is highly dependent on local failure [24]. In our simulations, we used the extreme LLS and ELS schemes mentioned previously, to model tissue failure in the nerve. A classic model [25] allows for a composite to be modeled as a chain of bundles, where the links of the chain act in series and the bundle fibrils act in parallel. Essentially, if all the fibrils, F, within any of the bundles, G, fails, then the composite, H, fails via

$$H_{m,n}(x) = 1 - [1 - G_n(x)]^m \quad \text{for } x \geqslant 0, \tag{8}$$

where n is the number of fibrils in parallel for a given bundle G in a composite with m bundles (Table 1). Our implementation was slightly modified in that we assumed that fibrils and thus bundles were tissue-spanning (i.e., $m = 1$) at both the tissue-bundle scale and at the bundle-fibril scale. A full treatment is given in Refs. [24,25] but, briefly, bundle failure equations have the form

$$\begin{aligned} G_1(x) &= F(x), \\ G_2(x) &= 2F(2x)F(x) - F(x)^2, \\ G_3(x) &= 6F(x)F\left(\frac{3x}{2}\right)F(3x) - 3F\left(\frac{3x}{2}\right)^2 F(x), \end{aligned} \tag{9}$$

where $F(x)$ is the familiar Weibull function (6).

Closed-form solutions for G with $n > 9$ become intractable, and those which include solutions for non-straight fibrils do not exist; thus, binning fibril behavior in a small set (11) was identified as a practical solution. As an example of an extension to this model which we will mention, but not explore here, a similar solution could be constructed for bond failure, within a single type I collagen alpha helix, according to

$$D_{m,n}(x) = 1 - [1 - C_3(x)]^n, \tag{10}$$

where D represents the failure probability function of three bound collagen alpha helices, C. This equation could be used to bridge scales C and D, (Fig. 1) where n in this case could be further compartmentalized into its approximately 1100 covalent peptide bonds within a single triple helix plus its variable (~50–100) crosslinks.

The mathematical descriptions of the ELS and LLS are given as follows. As the name implies, in ELS, when one fibril breaks, all the surviving fibrils share the remaining load equally. In LLS, fibrils neighboring a broken fibril sustain the majority of the load, shielding the other fibrils. This is the equivalent of a stress concentration factor. In simulations here, we used

$$K_r = 1 + \frac{r}{2}. \tag{11}$$

So in our example with 11 fibrils, in ELS, for one broken fibril, K for each remaining fibril was 11/10. But in LLS, K for the two fibrils nearest the broken one was 1.5, with the remaining nine having a $K = 1$. Since each simulation employed a random variable mapped into the Weibull distribution, sets of 10 simulations were run for each pair of

E_x and α. For each simulation the RMS error was calculated as

$$\mathrm{RMS} = \sqrt{\sum_{i=1}^{N} \frac{(\hat{\sigma}_i - \sigma_i)^2}{N}}, \tag{12}$$

where $\hat{\sigma}$ is the vector of experimental stress values and σ is the vector of simulated stress values. These were then contour mapped and the minima reported according to [57].

An aspect ratio, A, was defined for each failure curve as

$$A = \frac{\varepsilon(\mathrm{UTS}/2)}{\sigma_{\mathrm{UTS}}}, \tag{13}$$

where ε(UTS/2) is the width of the full failure curve taken at a height of one-half the ultimate tensile stress, σ_{UTS}.

For each sample, a total of 6000 simulations, each taking approximately 30 s on the Sun Blade-1000 (900 MHz, 2GB RAM) platform, were run. To compare results between the diabetic and control groups, Student's unpaired two-tailed t-tests were used, and p-values calculated for each comparison.

3. Results

While our primary objective of this work is to demonstrate that our modified Weibull–Harlow–Phoenix model is useful for relating the macroscopic failure behavior of soft biological tissue to the molecular scale modifications in diabetic tissue, we realize that future work in this area may include models employing a continuum mechanics approach. As a matter of convenience for those using such approaches, we have made a first approximation as to the shape of the toe region. The intent of this paper is primarily to determine tissue-morphology-based parameters, γ and a, rather than the polynomial parameters that follow.

Stress–strain curves were curve-fitted to quadratic equations

$$\sigma = c\varepsilon^2 + \mathrm{d}\varepsilon. \tag{14}$$

No constant term was included, because less than 0.5% of maximum stress was truncated and shifted in the toe region, since data were from nerves that had been previously strained. These results show that the quadratic term was significantly stronger ($p = 0.038$) in the diabetics (Table 3). This trend was repeated when a cubic approximation was used. Using a cubic function to approximate the toe region, increased R^2 values of 0.998 and 0.999 for diabetics and controls, respectively, were found. A quartic model found increased R^2 values to greater than 0.999. A larger higher-order term implies that the onset of load happens more suddenly once a certain strain is reached, whereas a stronger contribution from the linear term implies that loading occurs more gradually.

Table 3
Model input parameters and model results for diabetic ($n = 8$) and control ($n = 6$) uniaxial testing and simulations

Model	Parameter	Diabetics	Controls
(a)	L_N (mm)	10.0 ± 0.0	10.0 ± 0.0
	D_N (mm)	1.18 ± 0.08	1.23 ± 0.07
	ε_L	0.11 ± 0.04*	0.25 ± 0.10
	ε_H	0.20 ± 0.05*	0.40 ± 0.18
	σ_L (MPa)	0.88 ± 0.40	0.96 ± 0.25
	σ_H (MPa)	2.83 ± 1.07	2.39 ± 0.60
	E_N (MPa)	25.9 ± 14.1	16.1 ± 5.8
	E_F (MPa)	365 ± 167*	169 ± 75
	A	0.050 ± 0.031*	0.171 ± 0.097
	W_v (kJ/m^3)	24.73 ± 23.17*	62.39 ± 33.88
(b) $\sigma = c\varepsilon^2 + \mathrm{d}\varepsilon$	c	71.1 ± 51.1*	23.3 ± 20.6
	d	1.49 ± 1.02	1.58 ± 0.52
	R^2	0.979 ± 0.014	0.983 ± 0.013
(c) $\sigma_\gamma = 0$	a	0.51 ± 0.12*	0.63 ± 0.06
	σ_a	0.12 ± 0.03	0.20 ± 0.10
	RMS	0.641 ± 0.272	0.457 ± 0.089
	R^2	0.998 ± 0.001	0.998 ± 0.001
(d) $\sigma_a = 0$	a	0.43 ± 0.09	0.53 ± 0.09
	σ_γ	1.51 ± 0.39	1.57 ± 0.17
	RMS	0.561 ± 0.235	0.107 ± 0.000
	R^2	0.987 ± 0.005	0.988 ± 0.002
(e) ELS	α	9.9 ± 5.50*	4.33 ± 3.67
	E_x	0.28 ± 0.07*	0.58 ± 0.25
	RMS	0.150 ± 0.130	0.162 ± 0.056
(f) LLS	α	21.8 ± 3.87*	10.17 ± 10.91
	E_x	0.30 ± 0.07*	0.73 ± 0.27
	RMS	0.288 ± 0.293	0.284 ± 0.143

(a) Whole nerve diameter, D_N strain and stress at the onset ε_L, σ_L and end ε_H, σ_H, of the linear region, whole nerve modulus, E_N and fibril modulus, E_F, used as input to the simulations. Aspect ratio A, was defined as the width-to-height ratio of the failure curves. Strain energy, $W_v = \int \sigma\,\mathrm{d}\varepsilon$ under the toe region is also shown. (b) Results of quadratic curve fitting of toe region (up to ε_L) of unaxial test data from diabetic and control whole rat sciatic nerves. (c) Results for RMS minimization with $\bar{a}$ and σ_a as parameters ($\sigma_\gamma = 0$). (d) Results for RMS minimization with $\bar{a}$ and σ_γ as parameters ($\sigma_a = 0$). (e) Results for RMS minimization of Weibull parameters, α and E_x under equal load sharing (ELS). (f) Results for RMS minimization of Weibull parameters, α and E_x under local load sharing (LLS).

To study the effects of actual fibril geometry, amplitude, a, and amplitude standard deviation, σ_a were found, up to ε_H, for eight diabetic and six control specimens. A typical result (Fig. 6) is shown, demonstrating that control tissues (Fig. 6a) had both higher amplitude averages and standard deviations than those of diabetics (Fig. 6b). To further examine the effects of actual fibril geometry, amplitude and angle standard deviation were also simulated to strains up to ε_H for each specimen. A typical result (Fig. 7) reveals a similar trend, with control specimens (Fig. 7a) requiring a larger amplitude and standard deviation than those of diabetics (Fig. 7b), to minimize RMS error.

The relative responses resulting from ELS vs. LLS assumptions in a typical control specimen can be seen in the contour plot of Fig. 8, which shows that to sustain a

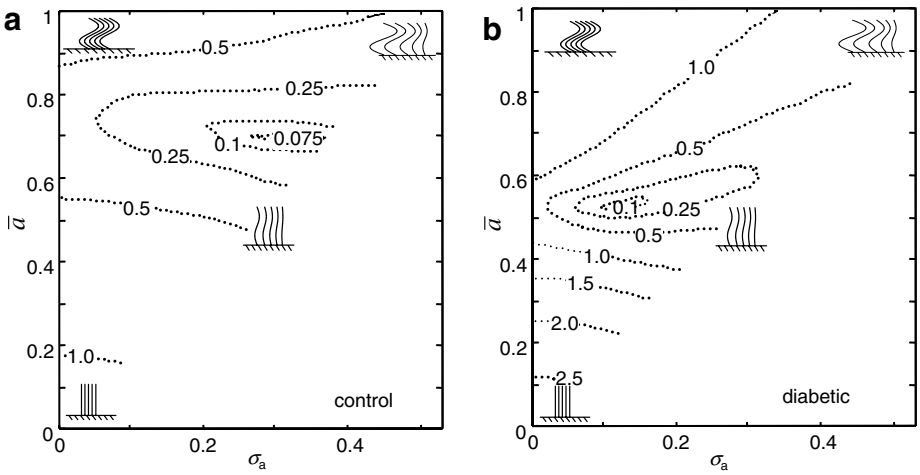

Fig. 6. RMS error contour plot of results from fitting a single rat sciatic nerve uniaxial stress–strain curve from (a) control and (b) diabetic specimens up to ε_H, with parameters $\bar{a}$ (average fibril amplitude) and σ_a (standard deviation of fibril amplitude) holding $\gamma = 0$. In all simulations, $\bar{\gamma} = 0$. The plot is only half-populated since, for example, in all simulations where $\bar{a} = 0$, $\sigma_a = 0$. Key features are that the combination of $\bar{a}$ and σ_a has been found that minimizes RMS error: $\bar{a} = 0.7$, $\sigma_a = 0.33$ for control and $\bar{a} = 0.525$, $\sigma_a = 0.115$ for diabetic. The four icons on the boundary of the contour plot depict the approximate fibril geometry used to generate that region.

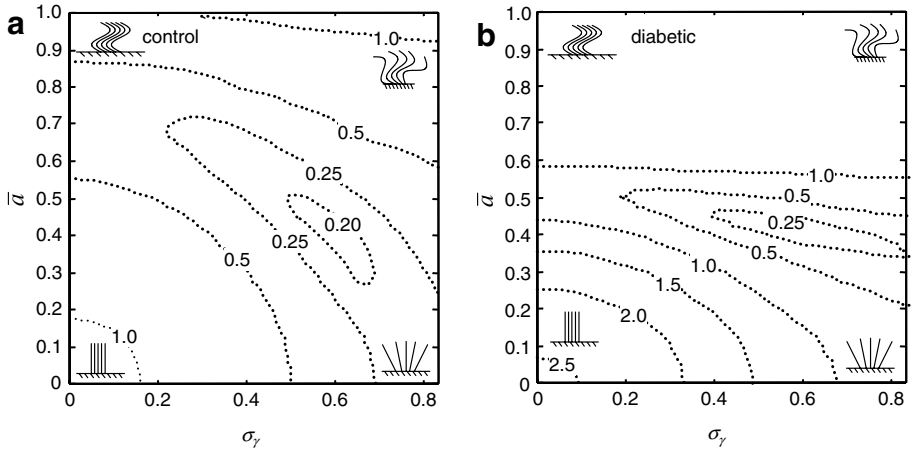

Fig. 7. RMS error contour plot of results from fitting a single rat sciatic nerve uniaxial stress–strain curve for (a) control and (b) diabetic specimens up to ε_H, with parameters $\bar{a}$ (average fibril amplitude) and σ_γ (standard deviation of fibril angle), holding $\sigma_a = 0$. In all simulations, $\bar{\gamma} = 0$. Generally speaking, larger amplitudes and variations in angle are found to best represent the more compliant control tissue, whereas smaller amplitudes and smaller variations in angle are found to best represent diabetic tissue. The four icons on the boundary of the contour plot depict the approximate fibril geometry used to generate that region.

given load, in the case of the LLS scenario (Fig. 8b) the fibrils must be stronger than in the ELS scenario (Fig. 8a). Values of E_x and α for all diabetic specimens were also plotted; a typical result for diabetic tissue (Fig. 9) demonstrates that application of the LLS model implies stronger fibrils for a given load, to fit experimental data. In this case, the ELS assumption resulted in lower local RMS errors, but to a lesser degree than was the case for the control data.

Goodness of fit, ϕ, was evaluated as the difference between the minimum RMS error value for each of the two models, normalized by the LLS error:

$$\phi = \frac{\mathrm{RMS}_{\mathrm{LLS}} - \mathrm{RMS}_{\mathrm{ELS}}}{\mathrm{RMS}_{\mathrm{LLS}}}. \tag{15}$$

The LLS model, in general, fit the diabetic failure curves better than the ELS model; the ELS model fit control failure curves better than the LLS model (Fig. 10). Across all samples, the ELS model had a lower RMS value; however, when we compare the two models with (15) we see that this difference is greater (i.e., relatively lower RMS ELS for controls compared to diabetics). This supports Hypothesis 3. The aspect ratio, A, was found to differ significantly between diabetic failure curves and control failure curves, 0.050 vs. 0.171 ($p < 0.05$) (Table 3a).

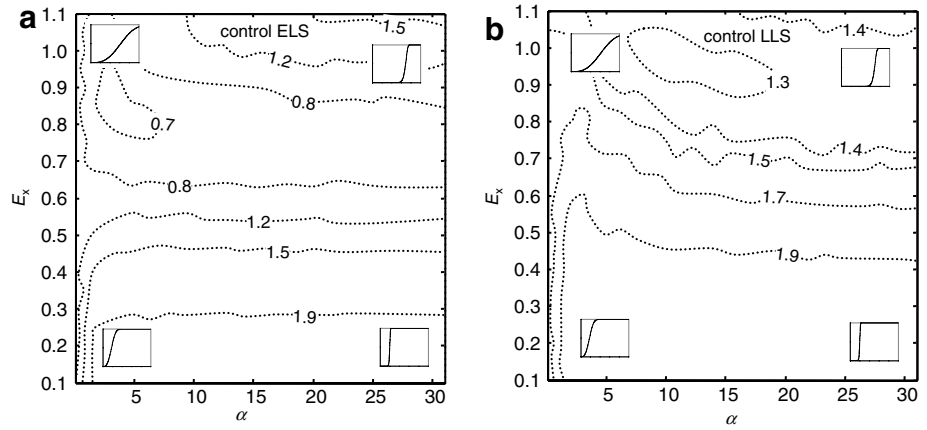

Fig. 8. RMS error contour plot of results of curves for varying Weibull parameters based on collagen fibril strengths to fit a typical stress–strain failure curve from a control animal for (a) equal load sharing and (b) local load sharing. In (b) local load sharing the fibrils must be stronger on average to carry the same global load. The four icons on the boundary of the contour plot depict the approximate shape of the Weibull cumulative distribution function used to generate that region.

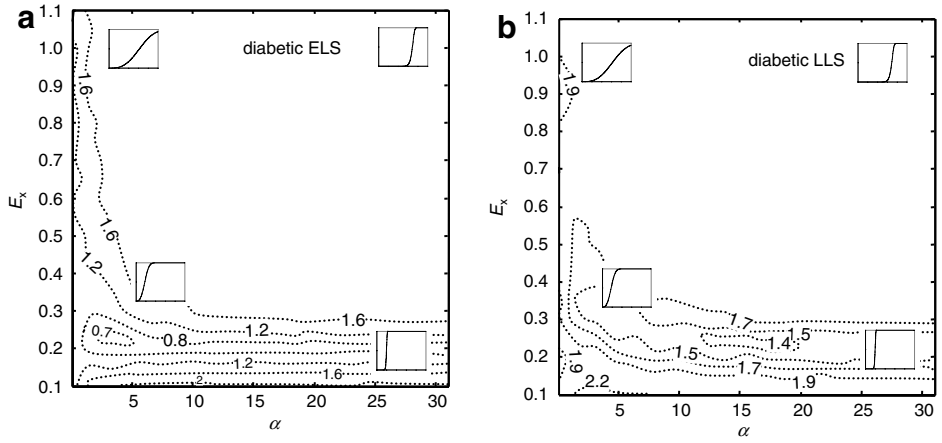

Fig. 9. RMS error contour plots of results of curves for varying Weibull parameters based on collagen fibril strengths to fit a typical stress–strain failure curve from a diabetic animal for (a) equal load sharing and (b) local load sharing. Notice that even though the diabetic tissue has a greater failure strength, its minimal E_x (normalized Weibull scale parameter) value is less than that of the control (Fig. 8) since its E_f (fibril modulus) is greater (Fig. 5). The four icons on the boundary of the contour plot depict the approximate shape of the Weibull cumulative distribution function used to generate that region.

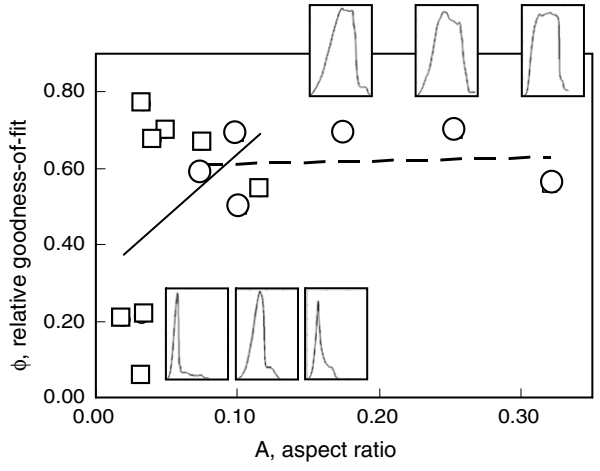

Fig. 10. A plot depicting relative goodness-of-fit, ϕ, (15) as a function of failure curve aspect ratio, A as defined in (13). Squares denote diabetic results and circles denote control results. Three diabetic and control stress–strain curves are shown. The solid line depicts a least-squares fit to the diabetic data. The dashed line is a least-squares fit to the control data.

4. Discussion

As may be seen from the results of Table 3, Hypothesis 1 is supported by experimental evidence. Diabetic nerve tissues exhibited a significantly ($p < 0.05$) greater shape parameter, α for ELS (9.88 vs. 4.33) and for LLS (21.81 vs. 10.17). The results of Table 3 also support Hypothesis 2; a significantly ($p < 0.05$) lower modulus-normalized scale parameter, E_x, was found in diabetic vs. control tissues, for both ELS (0.28 vs. 0.58) and for LLS (0.30 vs. 0.73) assumptions. Hypothesis 3 was also supported by experimental and numerical findings; the normalized RMS error for the LLS model for diabetics had a relatively lower error than the ELS model. This implies that the diabetic nerves behaved in a more brittle manner. Likewise, in support of Hypothesis 3, the failure data for the control nerves tended to fit the ELS model better than it did the LLS model. This implies that the ability of the ELS model to shield or protect unbroken fibrils from local overload in

the vicinity of failed fibrils may offer insight into the micro- and nanoscale failure processes within collagenous tissue.

The broader implications of these results are as follows. For more highly correlated fibrils, either due to an increased number of crosslinks or due to higher correlations within individual triple helices, peripheral nerve would be more likely to fail with elevated endoneurial fluid pressure (EFP). This relationship is suggested by prior literature [58], though we have not studied the degree of the effect of this reduction in failure stress in light of very classic EFP data.

Fibril modulus was assigned based upon whole-tissue response and assumed collagen volume and packing fractions. Ideally, a smaller specimen on the order of just a few fibrils, or a single bundle of almost purely collagenous epineurium could be taken from the nerve sample and tested separately to obtain a fibril modulus. This approach would not only allow insight into the degree to which glycation affects fibril properties, but would also serve to narrow the bounds on the load-sharing rule. As additional information becomes available with advanced imaging and labeling technologies, our methodology will be applied more readily.

There is extensive literature on the molecular modeling of the elastic properties of collagen, see e.g., Refs. [59–61] and failure mechanics of collagen, e.g., Ref. [52]. The incorporation of the results of such approaches would augment our model by serving as a front-end refinement to our linear elastic model of individual fibrils, as well as a source of failure distribution data to our Weibull curves. The effect of employing molecular mechanics simulations might improve the accuracy of our model, and could serve to refine a bundle model of glycated collagen-reinforced tissue to a model intermediate to extreme LLS and ELS behavior.

In previous work [19], we considered the sciatic nerve as a pressure vessel where the transverse properties of this pressure-vessel structure were considered. The main underlying assumption is that collagen is the major load-carrying component of nerve. Similar approximations have been made for other soft-tissue models based primarily on volume-fraction assumptions. For example, Ault and Hoffman [63] assume that the protein elastin contributes negligibly to mechanical behavior of tendon due to its low volume fraction. A similar argument may be made for our neglect of the contribution of cellular material in nerve. Experimental values of cellular material in individual axons [62] have shown that the maximum force individual neurons can sustain is on the order of 1 nN. With approximately half a million neurons in a sciatic nerve, this represents a total force of less than a mN, or a contribution three orders of magnitude lower than the forces generated by the collagen matrix.

Neither continuum nor multiscale models developed to date can provide the complete description we show here, though each has specific strengths. Continuum models are essentially phenomenological, as is our polynomial curve-fitting (Table 3) model, while the stochastic failure model presented here registers individual substructures, indexes them by their location within the material, and assigns individual collagen fibrils, a mathematical contribution in the stress–strain curve, based on data from the structures themselves. Attempts to model the viscoelastic properties of peripheral nerve with continuum-mechanics-based approaches [21,65], have the central shortcoming of inability to incorporate fibril load sharing. Multiscale models, some even using seven or more parameters [66], have been used to span the macro–microscale dimensions, in tendon. As other authors have pointed out, however, these methods neglect what may occur in the case of local failure from overloading due to stochastic nature of the material. A micromechanics-based model for mechanical properties of connective tissue [67], and even an attempt to quantify the toe region-to-failure curve for low volume fraction reconstituted ECM [68] have also been proposed. But the present model goes beyond that of traditional continuum approaches for modeling nonlinear tissues, see e.g., Refs. [69,70], and gives us a better understanding of how the molecular scale of tissue affects global properties for the purpose of predicting how and where failure is likely to occur.

One common difficulty in reporting results of soft tissue experimental mechanics is the decision on where to mark the "zero load" condition. Two methods include defining zero load at the precision limit of measurement of the device recording load, or selecting some fraction of *in vivo* strain to define zero load. The former has the difficulty that the mass of the specimen is likely larger than the precision limit of the measuring device; the latter has the difficulty that anatomical posture affects *in vivo* strain, and thus is not an unambiguous or repeatable value.

In our tensile apparatus, specimens were suspended above an analytic balance. The balance was tared while the specimen was still slack, leaving a small fraction of the mass supported by the scale. The mass of each specimen was approximately 100 μN. If one-tenth of the specimen was supported by the scale, this represents a force of 10 μN or ~10E−6 of our maximum loads of around 10 N. One might like to know the true load during tensile testing normalized to in vivo values. Such a method would involve non-invasive or minimally invasive imaging and sample marking prior to sample excision, coupled with a method of replicating the true *in vivo* loading mode. Here, we have placed the zero load condition at 0.5% of maximum load. This was identified as a simple, convenient, consistent and repeatable method.

The terms most likely affected by our choice of zero load are the coefficient c of (14) as well as the angle, γ and amplitude a terms. However, since a greater fraction of low-load toe region was eliminated from the control specimens as compared with diabetic specimens, this would only exaggerate the effects found in Table 3. Another term likely to be affected by our choice of zero load is the strain-energy term, W. The strain-energy term is less sensitive to the selection of absolute zero than those mentioned above. If the toe region were allowed to extend further to the left, giving additional area under the stress strain curve, the ds term would be small due to the very small slope (ds/de)

of the curve. This change would be small compared to the total area under the curve, regardless of the duration of the straining. For the results of our experiments, the effects would be exaggerated since the control nerves tended to have more protracted failure regions.

The modeling described here, in mapping the failure mechanics of the tissue Weibull statistics, follows from classic literature on rope, cable, and other engineered materials [71,72]. It is likely in the future that adaptation of such models will become more common, as detailed investigation of the structure of tissue becomes possible. Indeed, the biomechanics literature has shown a recent increase in the application of micromechanics tissue models, see e.g., Refs. [67,68,73]. Indeed, our work can explain the recent findings [74] demonstrating that for collagenous tissue such as bovine pericardium, that the stiffness of actual collagen fibrils is not measured until ~10–15% strain.

Recent activity in failure mechanics modeling to extend the ELS and LLS load sharing strategies [75,76], to greater numbers of fibrils and with novel strategies for parameterizing behavior that falls somewhere between the two extremes, has appeared. An interesting extension of the current work would be the application of these methods of Refs. [63,64] to problems of biological relevance, especially in the fields of disease modeling and tissue engineering.

In conclusion, the central advantage of a micromechanics approach is that histological and anatomical data can be used directly in mechanics models, and can further allow direct use of biochemical data in prediction of mechanical behavior. In the specific case of peripheral nerve, alterations in function have been linked with axially several stretching; these include membrane potential [77], compound nerve action potential [78], blood flow [79], and nerve conduction velocity [80]. When peripheral nerve is compressed with a tourniquet [79] nerve conduction velocity also diminishes. The efforts initiated here may prove useful in interrogating a number of functional losses in glycated peripheral nerves. More accurate experimental data on intra- and interfibril mechanical properties as well as more extensive nanomorphological data to resolve our tissue-spanning hypothesis will allow better approximations for load sharing and fiber recruitment during load, and ultimately, prediction of mechanical properties of collagenous tissues undergoing biochemical alterations.

Acknowledgements

This work was supported by the W.M. Keck Foundation, the Whitaker Foundation and by an NSF PECASE grant (Sastry); this funding is gratefully acknowledged.

References

[2] Hadley J, Malik N, Meek K. Collagen as a model system to investigate the use of aspirin as an inhibitor of protein glycation and crosslinking. Micron 2001;32(3):307–15.

[3] Odetti P, Aragno I, Rolandi R, Garibaldi S, Valentini S, Cosso L, et al. Scanning force microscopy reveals structural alterations in diabetic rat collagen fibrils: role of protein glycation. Diabetes Metab Res Rev 2000;16(2):74–81.

[4] Sajithlal GB, Chithra P, Chandrakasan G. Advanced glycation end products induce crosslinking of collagen in vitro. Biochim Biophys Acta 1998;1407(3):215–24.

[5] Vasan S, Zhang X, Kapurniotu A, Bernhagen J, Teichberg S, Basgen J, et al. An agent cleaving glucose-derived protein crosslinks in vitro and in vivo. Nature 1996;382(6588):275–8.

[6] Yang SZ, Litchfield JE, Baynes JW. AGE-breakers cleave model compounds, but do not break Maillard crosslinks in skin and tail collagen from diabetic rats. Arch Biochem Biophys 2003;412(1):42–6.

[7] Zieman SJ, Kass DA. Advanced glycation endproduct crosslinking in the cardiovascular system: potential therapeutic target for cardiovascular disease. Drugs 2004;64(5):459–70.

[8] Reihsner R, Melling M, Pfeiler W, Menzel EJ. Alterations of biochemical and two-dimensional biomechanical properties of human skin in diabetes mellitus as compared to effects of in vitro non-enzymatic glycation. Clin Biomech 2000;15(5):379–86.

[9] Reihsner R, Menzel EJ. Two-dimensional stress-relaxation behavior of human skin as influenced by non-enzymatic glycation and the inhibitory agent aminoguanidine. J Biomech 1998;31(11):985–93.

[10] Macey LR, Kana SM, Jingushi S, Terek RM, Borretos J, Bolander ME. Defects of early fracture-healing in experimental diabetes. J Bone Joint Surg Am 1989;71(5):722–33.

[11] Feldman EL. Oxidative stress and diabetic neuropathy: a new understanding of an old problem. J Clin Invest 2003;111(4):431–3.

[12] Fu MX, Wells-Knecht KJ, Blackledge JA, Lyons TJ, Thorpe SR, Baynes JW. Glycation, glycoxidation, and cross-linking of collagen by glucose. Kinetics, mechanisms, and inhibition of late stages of the Maillard reaction. Diabetes 1994;43(5):676–83.

[13] King RH. The role of glycation in the pathogenesis of diabetic polyneuropathy. Mol Pathol 2001;54(6):400–8.

[14] Seyer JM, Kang AH, Whitaker JN. The characterization of Type I and Type III collagens from human peripheral nerve. Biochim Biophys Acta 1977;492:415–25.

[15] Fujii K, Tsuji M, Murota K. Isolation of peripheral nerve collagen. Neurochem Res 1986;11(10):1439–46.

[16] Dumanian GA, McClinton MA, Brushart TM. The effects of free fat grafts on the stiffness of the rat sciatic nerve and perineural scar. J Hand Surg-Am 1999;24A(1):30–6.

[17] Wang H, Layton BE, Sastry AM. Nerve collagens from diabetic and nondiabetic Sprague–Dawley and biobreeding rats: an atomic force microscopy study. Diabetes Metabol Res Rev 2003;19(4):288–98.

[18] Layton BE, Sastry AM, Wang H, Sullivan KA, Feldman EL, Komorowski TE, et al. Differences between collagen morphologies, properties and distribution in diabetic and normal biobreeding and Sprague–Dawley rat sciatic nerves. J Biomech 2004;37(6):879–88.

[19] Layton BE, Sastry AM. A mechanical model for collagen fibril load sharing in peripheral nerve of diabetic and non-diabetic rats. ASME J Biomech Eng 2004;126:803–14.

[20] Abrams RA, Butler JM, Bodine-Fowler S, Botte MJ. Tensile properties of the neurorrhaphy site in the rat sciatic nerve. J Hand Surg [Am] 1998;23(3):465–70.

[21] Wall EJ, Kwan MK, Rydevik BL, Woo SL, Garfin SR. Stress relaxation of a peripheral nerve. J Hand Surg [Am] 1991;16(5):859–63.

[22] Sasaki N, Odajima S. Stress–strain curve and Young's modulus of a collagen molecule as determined by the X-ray diffraction technique. J Biomech 1996;29(5):655–8.

[23] Pins GD, Christiansen DL, Patel R, Silver FH. Self-assembly of collagen fibers. Influence of fibrillar alignment and decorin on mechanical properties. Biophys J 1997;73(4):2164–72.

[24] Harlow DG, Phoenix SL. Chain-of-bundles probability model for strength of fibrous materials 2. Numerical study of convergence. J Compos Mater 1978;12(July):314–34.

[25] Harlow DG, Phoenix SL. Chain-of-bundles probability model for strength of fibrous materials 1. Analysis and conjectures. J Compos Mater 1978;12(April):195–214.
[26] Danielson HE. The statistical theory of the strength of bundles of threads. I. Proc Roy Soc (Lond A) 1945;183:405–35.
[27] Brownlee M. Glycation products and the pathogenesis of diabetic complications. Diabetes Care 1992;15(12):1835–43.
[28] Makita Z, Vlassara H, Cerami A, Bucala R. Immunochemical detection of advanced glycosylation end products in vivo. J Biol Chem 1992;267(8):5133–8.
[29] Ahmed N, Argirov OK, Minhas HS, Cordeiro CAA, Thornalley PJ. Assay of advanced glycation endproducts (AGEs): surveying AGEs by chromatographic assay with derivatization by 6-aminoquinolyl-*N*-hydroxysuccinimidyl-carbamate and application to *N*-epsilon-carboxymethyl-lysine- and *N*-epsilon-(1-carboxyethyl)lysine-modified albumin. Biochem J 2002;364:1–14.
[30] Vlassara H, Palace MR. Diabetes and advanced glycation endproducts. J Int Med 2002;251(2):87–101.
[31] Bai P, Phua K, Hardt T, Cernadas M, Brodsky B. Glycation alters collagen fibril organization. Connect Tissue Res 1992; 28(1–2):1–12.
[32] Benazzoug Y, Borchiellini C, Labat-Robert J, Robert L, Kern P. Effect of high-glucose concentrations on the expression of collagens and fibronectin by fibroblasts in culture. Exp Gerontol 1998;33(5):445–55.
[33] Muona P, Peltonen J, Jaakkola S, Uitto J. Increased matrix gene expression by glucose in rat neural connective tissue cells in culture. Diabetes 1991;40(5):605–11.
[34] Muona P, Jaakkola S, Zhang RZ, Pan TC, Pelliniemi L, Risteli L, et al. Hyperglycemic glucose concentrations up-regulate the expression of type VI collagen in vitro. Relevance to alterations of peripheral nerves in diabetes mellitus. Am J Pathol 1993;142(5): 1586–97.
[35] Muona P, Jaakkola S, Salonen V, Peltonen J. Diabetes induces the formation of large diameter collagen fibrils in the sciatic nerves of BB rats. Matrix 1989;9(1):62–7.
[36] Bradley JL, King RH, Muddle JR, Thomas PK. The extracellular matrix of peripheral nerve in diabetic polyneuropathy. Acta Neuropath 2000;99:539–46.
[37] Halme T, Vihersaari T, Penttinen R. Lysyl oxidase activity and synthesis of desmosines in cultured human aortic cells and skin fibroblasts: comparison of cell lines from control subjects and patients with the Marfan syndrome or other annulo-aortic ectasia. Scand J Clin Lab Invest 1986;46(1):31–7.
[38] Yamauchi M, London RE, Guenat C, Hashimoto F, Mechanic GL. Structure and formation of a stable histidine-based trifunctional cross-link in skin collagen. J Biol Chem 1987;262(24):11428–34.
[39] Cooper ME. Importance of advanced glycation end products in diabetes-associated cardiovascular and renal disease. Am J Hypertens 2004;17(12 Pt 2):31S–8S.
[40] Stitt AW, Moore JE, Sharkey JA, Murphy G, Simpson DA, Bucala R, et al. Advanced glycation end products in vitreous: Structural and functional implications for diabetic vitreopathy. Invest Ophthalmol Vis Sci 1998;39(13):2517–23.
[41] Sensi M, Pricci F, Andreani D, Di Mario U. Advanced nonenzymatic glycation endproducts (AGE): their relevance to aging and the pathogenesis of late diabetic complications. Diabetes Res 1991;16(1):1–9.
[42] Tanaka S, Avigad G, Brodsky B, Eikenberry EF. Glycation induces expansion of the molecular packing of collagen. J Mol Biol 1988;203(2):495–505.
[43] Thornalley PJ, Battah S, Ahmed N, Karachalias N, Agalou S, Babaei-Jadidi R, et al. Quantitative screening of advanced glycation endproducts in cellular and extracellular proteins by tandem mass spectrometry. Biochem J 2003;375(Pt 3):581–92.
[44] Monnier VM, Kohn RR, Cerami A. Accelerated age-related browning of human collagen in diabetes mellitus. Proc Natl Acad Sci USA 1984;81(2):583–7.
[45] Malik NS, Moss SJ, Ahmed N, Furth AJ, Wall RS, Meek KM. Ageing of the human corneal stroma: structural and biochemical changes. Biochim Biophys Acta 1992;1138(3):222–8.
[46] Araki N, Ueno N, Chakrabarti B, Morino Y, Horiuchi S. Immunochemical evidence for the presence of advanced glycation end products in human lens proteins and its positive correlation with aging. J Biol Chem 1992;267(15):10211–4.
[47] Meerwaldt R, Graaff R, Oomen PH, Links TP, Jager JJ, Alderson NL, et al. Simple non-invasive assessment of advanced glycation endproduct accumulation. Diabetologia 2004;47(7):1324–30.
[48] Nagaraj RH, Sell DR, Prabhakaram M, Ortwerth BJ, Monnier VM. High correlation between pentosidine protein cross-links and pigmentation implicates ascorbate oxidation in human lens senescence and cataractogenesis. Proc Natl Acad Sci USA 1991;88(22):10257–61.
[49] Daniels HE. The statistical theory of the strength of bundles of threads I. Proc R Soc Lond Ser A-Math Phys Sci 1945;183(995): 405–35.
[50] Ushiki T, Ide C. Three-dimensional organization of the collagen fibrils in the rat sciatic nerve as revealed by transmission- and scanning electron microscopy. Cell Tissue Res 1990;260(1): 175–84.
[51] Pins GD, Huang EK, Christiansen DL, Silver FH. Effects of static axial strain on the tensile properties and failure mechanisms of self-assembled collagen fibers. J Appl Polym Sci 1997;63(11):1429–40.
[52] Parkinson J, Brass A, Canova G, Brechet Y. The mechanical properties of simulated collagen fibrils. J Biomech 1997;30(6): 549–54.
[53] Christiansen DL, Huang EK, Silver FH. Assembly of type I collagen: fusion of fibril subunits and the influence of fibril diameter on mechanical properties. Matrix Biol 2000;19(5):409–20.
[54] Hulmes DJS, Wess TJ, Prockop DJ, Fratzl P. Radial packing, order, and disorder in collagen fibrils. Biophys J 1995;68(5):1661–70.
[55] Hulmes DJ. Building collagen molecules, fibrils, and suprafibrillar structures. J Struct Biol 2002;137(1–2):2–10.
[56] Makita Z, Vlassara H, Cerami A, Bucala R. Immunochemical detection of advanced glycosylation end products in vivo. J Biol Chem 1992;267(8):5133–8.
[57] Bevington PR, Robinson DK. Data reduction and error analysis for the physical sciences. 3rd ed., vol. xi. Boston, MA: McGraw-Hill; 2003. 320 p.
[58] Myers RR, Costello ML, Powell HC. Increased endoneurial fluid pressure in galactose neuropathy. Muscle Nerve 1979;2(4):299–303.
[59] Freeman JW, Silver FH. Elastic energy storage in unmineralized and mineralized extracellular matrices (ECMs): a comparison between molecular modeling and experimental measurements. J Theor Biol 2004;229(3):371–81.
[60] Misof K, Rapp G, Fratzl P. A new molecular model for collagen elasticity based on synchrotron X-ray scattering evidence. Biophys J 1997;72(3):1376–81.
[61] Lorenzo AC, Caffarena ER. Elastic properties, Young's modulus determination and structural stability of the tropocollagen molecule: a computational study by steered molecular dynamics. J Biomech 2005;38(7):1527–33.
[62] Fass JN, Odde DJ. Tensile force-dependent neurite elicitation via anti-beta 1 integrin antibody-coated magnetic beads. Biophys J 2003;85(1):623–36.
[63] Ault HK, Hoffman AH. A composite micromechanical model for connective tissues. 1. Theory. J Biomech Eng-Trans ASME 1992;114(1):137–41.
[64] Ault HK, Hoffman AH. A composite micromechanical model for connective tissues. 2. Application to rat tail tendon and joint capsule. J Biomech Eng-Trans ASME 1992;114(1):142–6.
[65] Toby EB, Rotramel J, Jayaraman G, Struthers A. Changes in the stress relaxation properties of peripheral nerves after transection. J Hand Surg [Am] 1999;24(4):694–9.
[66] Hurschler C, Loitz-Ramage B, Vanderby Jr R. A structurally based stress-stretch relationship for tendon and ligament. J Biomech Eng 1997;119(4):392–9.

[67] Parry DA. The molecular and fibrillar structure of collagen and its relationship to the mechanical properties of connective tissue. Biophys Chem 1988;29(1–2):195–209.
[68] Roeder BA, Kokini K, Sturgis JE, Robinson JP, Voytik-Harbin SL. Tensile mechanical properties of three-dimensional type I collagen extracellular matrices with varied microstructure. J Biomech Eng 2002;124(2):214–22.
[69] Haut RC, Little RW. Constitutive equation for collagen fibers. J Biomech 1972;5(5):423–30.
[70] Hoger A. The elasticity tensor of a transversely isotropic hyperelastic material with residual stress. J Elasticity 1996;42(2):115–32.
[71] Kolowrocki K. Asymptotic approach to reliability evaluation of rope transportation system. Reliab Eng Syst Saf 2001;71(1):57–64.
[72] Perry RJ. Estimating strength of the Williamsburg Bridge suspension cables. Am Stat 1998;52(3):211–7.
[73] Hurschler C, LoitzRamage B, Vanderby R. A structurally based stress–stretch relationship for tendon and ligament. J Biomech Eng-Trans ASME 1997;119(4):392–9.
[74] Liao J, Yang L, Grashow J, Sacks MS. Molecular orientation of collagen in intact planar connective tissues under biaxial stretch. Acta Biomater 2005;1(1):45–54.
[75] Pradhan S, Chakrabarti BK, Hansen A. Crossover behavior in a mixed-mode fiber bundle model. Phys Rev E 2005;71(3).
[76] Hidalgo RC, Moreno Y, Kun F, Herrmann HJ. Fracture model with variable range of interaction. Phys Rev E 2002;65(4).
[77] Galbraith JA, Thibault LE, Matteson DR. Mechanical and electrical responses of the squid giant-axon to simple elongation. J Biomech Eng-Trans ASME 1993;115(1):13–22.
[78] Wall EJ, Massie JB, Kwan MK, Rydevik BL, Myers RR, Garfin SR. Experimental stretch neuropathy – changes in nerve-conduction under tension. J Bone Joint Surg-Br 1992;74(1):126–9.
[79] Ogata K, Naito M. Blood-flow of peripheral-nerve effects of dissection, stretching and compression. J Hand Surg-Br Eur 1986; 11B(1):10–4.
[80] Driscoll PJ, Glasby MA, Lawson GM. An in vivo study of peripheral nerves in continuity: biomechanical and physiological responses to elongation. J Orthop Res 2002;20(2):370–5.
[81] Takahara K, Sato Y, Okazawa K, Okamoto N, Noda A, Yaoi Y, et al. Complete primary structure of human collagen alpha 1 (V) chain. J Biol Chem 1991;266(20):13124–9.
[82] Traub W, Steinmann B. Structural study of a mutant type I collagen from a patient with lethal osteogenesis imperfecta containing an intramolecular disulfide bond in the triple-helical domain. FEBS Lett 1986;198(2):213–6.
[83] Rainey JK, Goh MC. A statistically derived parameterization for the collagen triple-helix. Protein Sci 2002;11(11):2748–54.
[84] Ottani V, Martini D, Franchi M, Ruggeri A, Raspanti M. Hierarchical structures in fibrillar collagens. Micron 2002;33(7–8): 587–96.
[85] Ushiki T, Ide C. Three-dimensional architecture of the endoneurium with special reference to the collagen fibril arrangement in relation to nerve fibers. Arch Histol Japon 1986;49(5):553–63.
[86] Puxkandl R, Zizak I, Paris O, Keckes J, Tesch W, Bernstorff S, et al. Viscoelastic properties of collagen: synchrotron radiation investigations and structural model. Philos Trans R Soc Lond B Biol Sci 2002;357(1418):191–7.